

# Giant spin Nernst effect in a two-dimensional antiferromagnet due to magnetoelastic coupling induced gaps and interband transitions between magnonlike bands

D.-Q. To<sup>1</sup>, C. Y. Ameyaw<sup>1</sup>, A. Suresh<sup>2</sup>, S. Bhatt<sup>2</sup>, M. J. H. Ku<sup>1,2</sup>, M. B. Jungfleisch<sup>2</sup>, J. Q. Xiao<sup>2</sup>, J. M. O. Zide<sup>1</sup>, B. K. Nikolić<sup>2,\*</sup> and M. F. Doty<sup>1,†</sup>

<sup>1</sup>Department of Materials Science and Engineering, University of Delaware, Newark, Delaware 19716, USA

<sup>2</sup>Department of Physics and Astronomy, University of Delaware, Newark, Delaware 19716, USA



(Received 18 May 2023; revised 15 August 2023; accepted 17 August 2023; published 30 August 2023)

We analyze theoretically the origin of the spin Nernst and thermal Hall effects in FePS<sub>3</sub> as a realization of a two-dimensional antiferromagnet (2D AFM). We find that a strong magnetoelastic coupling, hybridizing magnetic excitations (magnons) and elastic excitations (phonons), combined with time-reversal symmetry breaking, results in Berry curvature hotspots in the region of anticrossing between the two distinct hybridized bands. Furthermore, a large spin Berry curvature emerges due to *interband transitions between two magnonlike bands*, where a small energy gap is induced by magnetoelastic coupling between such bands that are *energetically distant* from anticrossings of hybridized bands. These nonzero Berry curvatures generate topological transverse transport (i.e., the thermal Hall effect) of hybrid excitations, dubbed magnon-polarons, as well as of the spin (i.e., the spin Nernst effect) carried by them, in response to an applied longitudinal temperature gradient. We investigate the dependence of the spin Nernst and thermal Hall conductivities on the applied magnetic field and temperature, unveiling a very large spin Nernst conductivity *even* at zero magnetic field. Our results suggest the FePS<sub>3</sub> AFM, which is already available in 2D form experimentally, as a promising platform to explore the topological transport of magnon-polaron quasiparticles at terahertz frequencies.

DOI: [10.1103/PhysRevB.108.085435](https://doi.org/10.1103/PhysRevB.108.085435)

## I. INTRODUCTION

Two-dimensional (2D) antiferromagnets (AFMs) [1] are attracting growing attention due to their potential application as material platforms for spintronics, spin-orbitronics, and spin-caloritronics [2–10]. Because the strong exchange interaction between their localized spins results in intrinsic terahertz frequency dynamics, AFMs are particularly promising for the development of devices with high operating speeds. For example, magnons in a 2D AFM can be employed to store and transfer terahertz frequency information without Joule heating due to the absence of a charge current or a stray field. Such materials can also provide efficient spin-transport channels in spintronic devices with low energy consumption [11–16]. Despite these advantages, the use of magnons in 2D AFMs as a part of realistic devices is severely limited by the lack of efficient ways to generate and manipulate magnon excitations. The hybridization of magnons and phonons may provide a path toward coherent control of magnons in 2D AFM material via a manipulation of the hybridized states [17–21]. For instance, it has been shown that one can electrically generate magnon spin current through the interaction between magnons and phonons [22,23]. Conversely, it has also been shown that the dynamics of a phonon can be controlled via its interaction with a magnon [24–26].

Magnons and phonons are the collective and charge-neutral excitations of localized spins and lattice vibrations, respectively. They behave as bosonic quasiparticles, obeying the Bose-Einstein distribution function at finite temperature with zero chemical potential in equilibrium due to their nonconserved number. Strong coupling between a magnon and a phonon results in a hybridized state that includes both spin and lattice collective excitations in a single coherent mode [27–31]. As a result, a new type of quasiparticle, dubbed the magnon-polaron [32,33], is formed. The intriguing and nontrivial emergent properties of magnon-polarons provide a possible foundation for novel devices with unique optical and electrical functionalities [34–40]. In particular, the hybridization of magnons and phonons to create a magnon-polaron can generate finite Berry and spin (generalized) Berry curvatures concentrated around anticrossing regions [28–31] of the magnon and phonon bands. These Berry curvatures then lead to nontrivial topological transverse transport—the magnon thermal Hall effect (THE) and magnon spin Nernst effect (SNE)—which have attracted a lot of attention [27–31,33,41–48]. In particular, recent studies have demonstrated [32,40,49–52] possibly strong magnon-phonon coupling in FePS<sub>3</sub> as the realization of 2D AFM. This, together with the experimentally accessible 2D form of this material [33], makes FePS<sub>3</sub> a great candidate for investigation of magnon THE and SHE.

Let us recall that the magnon THE [43] refers to a phenomenon that occurs when a temperature gradient applied to a magnetic material generates transverse thermal transport of magnons, perpendicular to both the temperature gradient

\*bnikolic@udel.edu

†doty@udel.edu

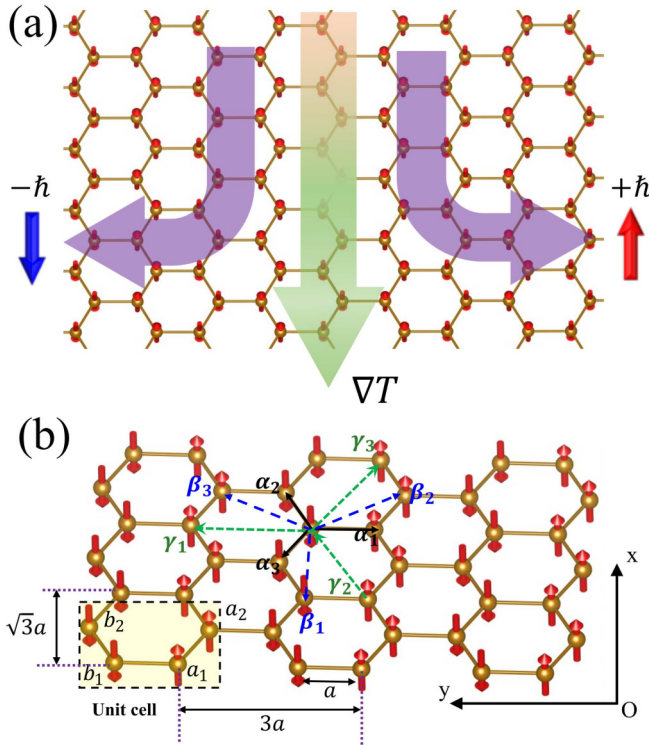


FIG. 1. (a) Schematic view of the magnon SNE in a 2D AFM where transverse flow of magnons carrying opposite out-of-plane spins ( $\pm \hbar$ ) is induced by temperature gradient  $\nabla T$  along the longitudinal direction [27]. (b) The quasi-2D lattice of FePS<sub>3</sub> formed by Fe atoms. The arrows indicate the direction of the localized spins within the zigzag AFM phase considered in this paper. Here,  $\alpha_i$ ,  $\beta_i$ , and  $\gamma_i$  ( $i = 1, 2, 3$ ) are the vectors joining the nearest, second-nearest, and third-nearest neighbors, respectively. A unit cell contains four Fe atoms forming a rectangularly shaped BZ with periodicity in real space that is  $\sqrt{3}a$  or  $3a$  long in the  $x$  or  $y$  direction (where  $a$  is the lattice constant), respectively.

and the magnetization. The magnon SNE [27], which is analogous to the electronic spin Hall effect (SHE) [53,54] where electrons of opposite spin travel in opposite directions transverse to applied unpolarized charge current, involves the flow of magnons instead of electrons carrying opposite spin flow in opposite directions perpendicular to the temperature gradient [Fig. 1(a)]. The magnon SNE is made possible by the existence of two magnon species within the AFM carrying opposite spin polarization [27]. Recent studies have shown that the magnon SNE can be observed in the following: collinear antiferromagnets [27,41,55] on a honeycomb lattice, where the Dzyaloshinskii-Moriya interaction (DMI) acting [56] on magnons plays an analogous role to that played by spin-orbit coupling (SOC) [53,54] for electrons in the SHE; noncollinear antiferromagnets [47,57], even without any SOC responsible for DMI, and in zero applied magnetic field; and collinear antiferromagnets [29–31] or ferrimagnets [28] with magnetoelastic coupling hybridizing magnon and phonon quasiparticle bands whose anticrossing regions are putatively crucial [28] to obtain the nonzero Berry and spin Berry curvature driving (see Sec. II B) transverse transport in the THE and SNE, respectively.

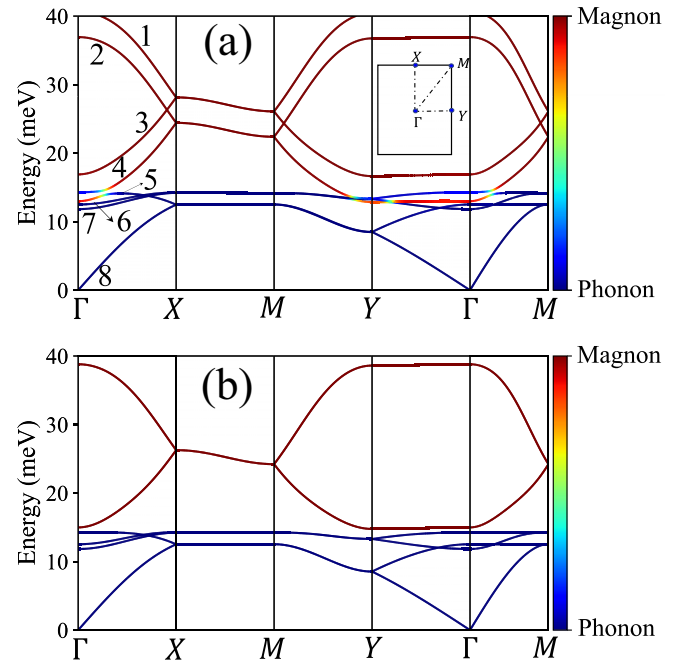


FIG. 2. (a) The hybridized magnon-phonon band structure of FePS<sub>3</sub> (Fig. 1), along the  $\Gamma$ - $X$ - $M$ - $Y$ - $\Gamma$ - $M$  high-symmetry path in the BZ marked in the inset, calculated for an applied magnetic field of  $B_z = 30$  T. The color scale bar encodes whether the bands have magnonlike, phononlike, or mixed character. The bands are labeled as bands 1–8 from the highest to the lowest energy. (b) The counterpart of (a), but in the absence of magnetoelastic coupling [ $H_m = 0$  in Eq. (4)] and for zero applied magnetic field [ $B_z = 0$  in Eq. (2)]. This means that red lines denote purely magnon bands and blue lines denote purely phonon bands of FePS<sub>3</sub>, without any hybridization between them being present.

In contrast, our study highlights a mechanism [31] where a significant spin Berry curvature can be induced in an energy window of magnonlike bands that is *energetically distant* [for example, the first and second bands in Fig. 2(a)] from the magnon-phonon hybridized bands and their anticrossing within a collinear AFM. The magnonlike bands possess a small phonon character (Fig. S2(d) in the Supplemental Material (SM) [58]) over the entire Brillouin zone (BZ), which causes opening of slight band gaps between them (Fig. S2(b) in the SM [58]). These band gaps are actually *smaller* than the anticrossing gap between magnonlike and phononlike bands (Fig. S2(b) in the SM [58]). The *smallness* of band gaps between magnonlike bands (Figs. S2(b) and S3(b) in the SM [58]) and phonon-mediated interband transitions [31] between them lead to significant spin Berry curvature (Fig. 5) and, thereby, the possibility of a giant SNE in the FePS<sub>3</sub> collinear AFM.

The paper is organized as follows. In Sec. II we introduce an effective Hamiltonian to capture the magnon-phonon hybridization within 2D AFMs belonging to the  $MPX_3$  ( $M = \text{Fe, Mn, Co, Ni}$ ;  $X = \text{S, Se}$ ) family hosting localized spins and their magnetic moments in a zigzag phase. The same section also reviews the theoretical framework of linear response theory that can be used to investigate the transverse transport of magnon-polaron quasiparticles. In Sec. III we discuss the

thus-generated SNE and THE for FePS<sub>3</sub>, including the dependence of the thermal Hall and spin Nernst conductivities on the applied magnetic field and temperature. We conclude in Sec. IV.

## II. MODELS AND METHODS

### A. 2D AFM Hamiltonian describing magnons, phonons, and their magnetoelastic coupling

The MPX<sub>3</sub> ( $M = \text{Fe, Mn, Co, Ni}$ ;  $X = \text{S, Se}$ ) family of materials are van der Waals magnets [1] forming layered structures that are weakly bound by van der Waals forces and possess a stable magnetic order even in the monolayer limit [59,60] because of a huge single-ion anisotropy energy [33,49,61–64]. In particular, Fig. 1 shows the layered structure of FePS<sub>3</sub> that is established solely by the Fe atoms. Within each layer, the Fe atoms are arranged in a honeycomblike lattice structure with “columns” of spins having opposite spin moments. We consider the FePS<sub>3</sub> magnetic structure in the so-called zigzag AFM phase in which a unit cell contains two pairs of equivalent atoms (i.e., having the same spin direction) that are labeled as  $a_i$  and  $b_i$  ( $i = 1, 2$ ), respectively. Due to the small value of the interlayer exchange interaction relative to the intralayer exchange interaction, these AFMs are, to a very good approximation, quasi-two-dimensional magnets even in the bulk [61,65–69]. The magnon-phonon hybridization in FePS<sub>3</sub> can therefore be investigated by focusing on the quasi-2D honeycomb structure of Fe atoms whose Hamiltonian can be written as

$$H = H_m + H_p + H_{mp}. \quad (1)$$

Here,  $H_m$  is the Hamiltonian of localized spins whose low-energy excited states are magnons [14],  $H_p$  is the phonon Hamiltonian, and  $H_{mp}$  is the term describing magnetoelastic coupling and thereby-induced hybridization of magnons and phonons. The term  $H_m$  is the anisotropic Heisenberg model [61,65–67,70]:

$$H_m = \sum_{i,j} J_{ij} \mathbf{S}_i \mathbf{S}_j + \Delta \sum_i (S_i^z)^2 + g\mu_B B_z \sum_i S_i^z, \quad (2)$$

where  $\mathbf{S}_i = (S_i^x, S_i^y, S_i^z)$  is the operator of total spin localized at a site  $i$  of the lattice;  $J_{ij}$  is the exchange coupling between localized spins at sites  $i$  and  $j$ ;  $\Delta$  is the easy-axis anisotropy energy; the Zeeman (third on the right) term takes into account coupling to the applied magnetic field  $B_z$  pointing along the  $z$  axis, which is perpendicular to the plane in Fig. 1;  $g$  is the Landé  $g$  factor; and  $\mu_B$  is the Bohr magneton. The sum  $\sum_{i,j}$  runs over all atom pairs in the lattice up to the third-nearest neighbor.

We take into account the magnetoelastic coupling by assuming that it acts only between magnons and out-of-plane phonons. Such an assumption is particularly relevant for FePS<sub>3</sub> 2D AFM, where out-of-plane phonon modes are closely aligned with the magnon modes in terms of energy and have been observed to hybridize with them under an applied magnetic field [49]. Therefore we focus only on the  $z$  component of the lattice vibrations, so that describing them with a simple harmonic oscillator model yields the following

effective phonon Hamiltonian [45,71]:

$$H_p = \sum_i \frac{(p_i^z)^2}{2M} + \frac{1}{2} \sum_{ij} u_i^z \Phi_{i,j}^z u_j^z. \quad (3)$$

Here,  $p_i^z$  and  $u_i^z$  are the operators of out-of-plane momentum and displacement of the atom at site  $i$  of the lattice, respectively;  $\Phi^z$  is a spring constant matrix; and  $M$  is the mass of the atom. Finally, for the magnetoelastic coupling, which generates hybridization of magnon and phonon bands [Fig. 2(a)], we adopt a Hamiltonian derived by Kittel [72] to linear order in the magnon amplitude and adapted [49,73] to magnons coupled to out-of-plane phonons in FePS<sub>3</sub>:

$$H_{mp} = -\xi \sum_i [\epsilon_i^{yz} (S_i^x S_i^z + S_i^z S_i^x) + \epsilon_i^{xz} (S_i^y S_i^z + S_i^z S_i^y)], \quad (4)$$

where  $\xi$  is the coupling strength and  $\epsilon_i^{xz}$  and  $\epsilon_i^{yz}$  are strain functions at the  $i$  site computed by averaging over the strain from nearest-neighboring ions

$$\epsilon_i^{\alpha\beta} = \frac{1}{N} \sum_j \epsilon_{ij}^{\alpha\beta}. \quad (5)$$

The two-ion strain tensor in the small-displacement approximation is given by [73,74]

$$\epsilon_{ij}^{\alpha\beta} = \frac{1}{2} [(r_i^\alpha - r_j^\alpha)(u_i^\beta - u_j^\beta) + (r_i^\beta - r_j^\beta)(u_i^\alpha - u_j^\alpha)], \quad (6)$$

where  $r_i^\alpha$  and  $u_i^\alpha$  are the  $\alpha$  components of the location vector in equilibrium and the displacement of the atom from equilibrium, respectively, for site  $i$  of the lattice.

The transformation of Eq. (1) into second-quantized notation is given in the SM [58]. Since this Hamiltonian is quadratic in the creation and annihilation operators for magnons and phonons, it can be exactly diagonalized to obtain the quasiparticle band structure in Fig. 2 for a magnon-polaron quasiparticle. For easy comparison, Fig. 2(b) plots nonhybridized magnon (red curves) and phonon (blue curves) bands in the absence of magnetoelastic coupling [ $H_m = 0$  in Eq. (4)] and for zero applied magnetic field [ $B_z = 0$  in Eq. (2)].

### B. Transverse thermal and spin transport in the linear response regime

Within the linear response theory, the equations describing transverse quasiparticle transport underlying the THE and SNE are given by [31,47,75–78]

$$j_y^Q = -\kappa_{xy} \partial_x T, \quad (7)$$

$$j_y^{S^z} = -\eta_{xy}^{S^z} \partial_x T, \quad (8)$$

where  $j_y^Q$  and  $j_y^{S^z}$  are the thermal current and spin current, respectively, flowing along the  $y$  axis in response to the temperature gradient  $\partial_x T$  applied along the  $x$  axis (Fig. 1). The coefficients of proportionality in Eqs. (7) and (8) are the thermal Hall conductivity

$$\kappa_{xy} = -\frac{k_B^2 T}{\hbar} \sum_{n=1}^N \int F_2(\rho_n) \Omega_n^z dk \quad (9)$$

and the spin Nernst conductivity

$$\eta_{xy}^{S^z} = \frac{k_B}{\hbar} \sum_{n=1}^N \int F_1(\rho_n) \Omega_{S^z, n}^z d\mathbf{k}. \quad (10)$$

Here,  $\rho_n = [e^{E_n/k_B T} - 1]^{-1}$  is the Bose-Einstein distribution function, with  $E_n$  being the eigenenergy of the  $n$ th band, which enters into the conductivity expressions through functions

$$F_1(\rho_n) = (1 + \rho_n) \ln(1 + \rho_n) - \rho_n \ln(\rho_n) \quad (11)$$

or

$$F_2(\rho_n) = (1 + \rho_n) \ln^2 \left( 1 + \frac{1}{\rho_n} \right) - \ln^2(\rho_n) - 2 \text{Li}_2(-\rho_n), \quad (12)$$

where  $\text{Li}_2$  is the polylogarithm function. Finally, the Berry  $\Omega_n(\mathbf{k})$  curvature and spin (generalized) Berry  $\Omega_{S^z, n}(\mathbf{k})$  curvature of the  $n$ th band are given by [31,47]

$$\Omega_n(\mathbf{k}) = \sum_{m \neq n} \frac{i\hbar^2 \langle n(\mathbf{k}) | \mathbf{v} | m(\mathbf{k}) \rangle \langle m(\mathbf{k}) | \sigma_3 | m(\mathbf{k}) \rangle \times \langle m(\mathbf{k}) | \mathbf{v} | n(\mathbf{k}) \rangle \langle n(\mathbf{k}) | \sigma_3 | n(\mathbf{k}) \rangle}{[\sigma_3^{nm} E_n(\mathbf{k}) - \sigma_3^{mm} E_m(\mathbf{k})]^2} \quad (13)$$

and

$$\Omega_{S^z, n}(\mathbf{k}) = \sum_{m \neq n} \frac{i\hbar^2 \langle n(\mathbf{k}) | \mathbf{j}^{S^z} | m(\mathbf{k}) \rangle \langle m(\mathbf{k}) | \sigma_3 | m(\mathbf{k}) \rangle \times \langle m(\mathbf{k}) | \mathbf{v} | n(\mathbf{k}) \rangle \langle n(\mathbf{k}) | \sigma_3 | n(\mathbf{k}) \rangle}{[\sigma_3^{nm} E_n(\mathbf{k}) - \sigma_3^{mm} E_m(\mathbf{k})]^2}, \quad (14)$$

where we use  $E_n(\mathbf{k})$  and  $|n(\mathbf{k})\rangle$  to denote the eigenvectors and eigenvalues, respectively, obtained from Colpa's diagonalization algorithm [79–82] (see the SM [58] for details);  $\mathbf{v} = (v_x, v_y, v_z)$  denotes the velocity vector operator;  $\mathbf{j}^{S^z}$  denotes the spin current tensor operator

$$\mathbf{j}^{S^z} = S^z \sigma_3 \mathbf{v} + \mathbf{v} \sigma_3 S^z, \quad (15)$$

and the  $\sigma_3$  matrix is given by

$$\sigma_3 = \begin{pmatrix} \mathbf{1}_{N \times N} & 0 \\ 0 & -\mathbf{1}_{N \times N} \end{pmatrix}, \quad (16)$$

where  $\mathbf{1}_{N \times N}$  is the  $N \times N$  identity matrix and  $\sigma_3^{nm} = \langle n(\mathbf{k}) | \sigma_3 | n(\mathbf{k}) \rangle$  is the  $n$ th diagonal element of  $\sigma_3$ . Thus evaluating Berry [Eq. (13)] and spin Berry [Eq. (14)] curvatures directly yields the thermal and spin Nernst conductivities, respectively.

### III. RESULTS AND DISCUSSION

#### A. Topological transport of magnon-polarons: Thermal Hall and spin Nernst effects

Topological transport will only emerge when two conditions are met. First, bands must have nonzero Berry curvature, which can emerge due to hybridization. Second, the integral of the Berry curvature over the Brillouin zone, which is known as the Chern number, must also be nonzero. We now show that both of these conditions are met in FePS<sub>3</sub> due to magnon-phonon coupling.

We first assume that FePS<sub>3</sub> is exposed to an applied magnetic field of 30 T. Figure 3(a) shows a zoom of the magnon-phonon hybridized bands from Fig. 2 focused on the fourth (predominantly magnon, as it is mostly red) and fifth (predominantly phonon, as it is mostly blue) bands in the energy window between 10 and 20 meV along the  $X$ - $\Gamma$ - $M$  path. These two bands are strongly coupled, which results in two anticrossings [Fig. 3(a)]. In the vicinity of these anticrossings, the eigenstates are hybridized,  $\psi_{\text{hybrid}} = \psi_{\text{magnon}} \pm \psi_{\text{phonon}}$ , with both magnon and phonon character. The presence of such superpositions is denoted by the bright green-yellow

color of the bands in the anticrossing region [Fig. 3(a)]. We note that *both* an applied magnetic field and magnetoelastic coupling between magnons and phonons are required for such hybridization and anticrossing to emerge: The magnetoelastic coupling provides the necessary interaction, while the magnetic field tunes the magnon and phonon bands toward energy degeneracy.

The hybridization of two distinct excitations leads to a finite Berry curvature. Let us recall that, e.g., hybridization of  $s$  and  $p$  states in HgTe/CdTe semiconductor quantum wells causes nontrivial topological properties for electrons at the

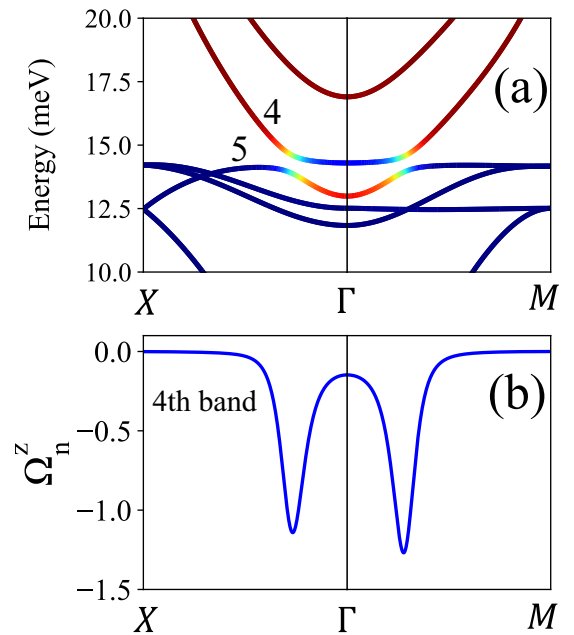


FIG. 3. (a) The hybridized magnon-phonon band structure of 2D FePS<sub>3</sub>, along the  $X$ - $\Gamma$ - $M$  high-symmetry path, calculated for an applied magnetic field of  $B_z = 30$  T. (b) The corresponding Berry curvature  $\Omega_n^z$  along the  $X$ - $\Gamma$ - $M$  path calculated for the fourth band in (a).

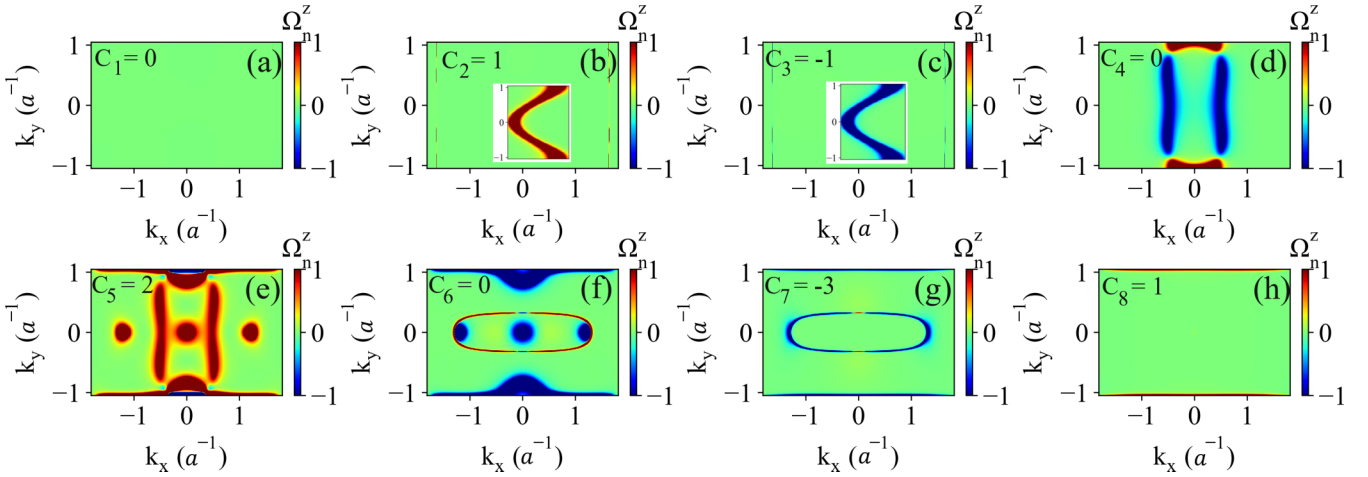


FIG. 4. The Berry curvature  $\Omega_n^z$  [Eq. (13)] computed for magnon-phonon bands (Fig. 2) of FePS<sub>3</sub> as a function of the in-plane wave vector  $(k_x, k_y)$  within the first BZ and using applied magnetic field  $B_z = 30$  T. (a)–(h) correspond to bands 1–8 denoted in Fig. 2. Their corresponding Chern number  $C_n$  ( $n = 1, 2, \dots, 8$ ) in Eq. (17) is provided in the upper left corner of each panel. The insets in (b) and (c) show zooms around  $k_x = -1.64$  ( $a^{-1}$ ), where the Berry curvature of the corresponding bands is nonzero.

Fermi level [83]. The physics here is analogous: In the region of the BZ where the magnon band (fourth band) and phonon band (fifth band) anticross, we expect nonzero Berry curvature. In contrast, we expect that away from the anticrossing regions, the Berry curvature should vanish because either band is dominated solely by magnon or phonon character. Figure 3(b), showing the Berry curvature [Eq. (13)] for the fourth band along the same  $X\text{-}\Gamma\text{-}M$  path, confirms this expectation as  $\Omega_n^z(\mathbf{k}) \neq 0$  in Fig. 3(b) only around the anticrossing regions identified in Fig. 3(a). In other words, the magnon and phonon bands acquire nonzero Berry curvature due to their hybridization via magnetoelastic coupling [Eq. (4)].

Figure 4 shows the Berry curvature for bands 1–8 in Fig. 2 as a function of the in-plane wave vector  $\mathbf{k} = (k_x, k_y)$ . In each panel, we also report the Chern number calculated as

$$C_n = \frac{1}{2\pi} \int_{\text{BZ}} \Omega_n^z(\mathbf{k}) dk_x dk_y. \quad (17)$$

These calculations were performed for an applied magnetic field  $B_z = 30$  T that causes the lowest magnon band to overlap with the out-of-plane optical phonon bands, as shown in Fig. 3(a). Nonzero Berry curvature is observed in the vicinity of anticrossing regions in the fourth, fifth, and sixth bands in the color plot. The first band [Fig. 4(a)] has zero Berry curvature everywhere, which obviously leads to zero Chern number. The fourth and sixth bands [Figs. 4(d) and 4(f)] have nonzero Berry curvature, but the integral of the Berry curvature over the entire BZ of these bands vanishes. As a result, the Chern number is zero, and these are topologically trivial bands. The other bands all have nonzero Chern number, with the sum of their Chern numbers obeying the sum rule,  $\sum_{i=1}^N C_i = 0$ , as expected for a Bogoliubov–de Gennes (BdG) Hamiltonian [28] (see the SM [58] for more details on the BdG Hamiltonian construction).

However, it is surprising and quite different from standard lore [27–30] that nonzero Berry curvature can be found for the second [Fig. 4(b)], third [Fig. 4(c)], and eighth [Fig. 4(h)] bands because these bands are well above or well below the energy window in which magnon and phonon bands become

degenerate in energy and anticross (Fig. 2). These bands all have nontrivial topology with a Chern number equal to  $\pm 1$ . The finite Berry curvature and nontrivial topological properties of these bands can be understood as follows. Magnetoelastic interaction facilitates coupling between magnon and phonon bands even when they are *not* energetically close together, so that magnon bands have small phononic character (see Figs. S2(c) and S2(d) in the SM [58] for details) and vice versa [31]. This effect can open a gap between two magnonlike bands [such as the second and third bands in Figs. 4(b) and 4(c)] at  $k_x = \pm 1.64$  ( $a^{-1}$ ), thereby making possible interband transitions between these two (see the inset of Fig. S2(b) in the SM [58] for details). Without magnetoelastic coupling, these magnon bands are degenerate, i.e., they cross each other at  $k_x = \pm 1.64$  ( $a^{-1}$ ) (Fig. S2(a) in the SM [58]). A precise quantum-mechanical interpretation of this picture can be obtained from the perturbation theory: The gap opening between the two magnonlike bands is due to perturbations from phonons, which appears as a second-order correction term

$$\delta E_{ij}^m \propto \sum_p [\bar{H}]_{mi,p} [\bar{H}]_{p,mj} \left[ \frac{1}{\bar{E}_{mi} - \bar{E}_p} + \frac{1}{\bar{E}_{mj} - \bar{E}_p} \right] \quad (18)$$

to the magnon band levels (for a derivation of Eq. (18), see the SM [58]). Here, the indices  $p$ ,  $mi$ , and  $mj$  indicate the phonon states which mediate interband transitions between magnon states  $i$  and  $j$ ;  $[\bar{H}]_{mi,p}$  ( $[\bar{H}]_{p,mj}$ ) describes the coupling between  $i$  magnon (phonon) band and phonon ( $j$  magnon) states; and  $\bar{E}_{mi}$ ,  $\bar{E}_{mj}$ , and  $\bar{E}_p$  are eigenenergies of  $i$  magnon,  $j$  magnon, and phonon states, respectively, as obtained from exact diagonalization of the bosonic magnon-phonon Hamiltonian (see the SM [58] for details). As a result, the Berry curvature of the second and third bands at around  $k_x = \pm 1.64$  ( $a^{-1}$ ), which is associated with the tiny avoided crossing points between the second and third magnonlike bands, *becomes finite*. An analogous effect occurs for the phonon bands. For instance, a magnon-mediated phonon-phonon interband transition between the seventh and

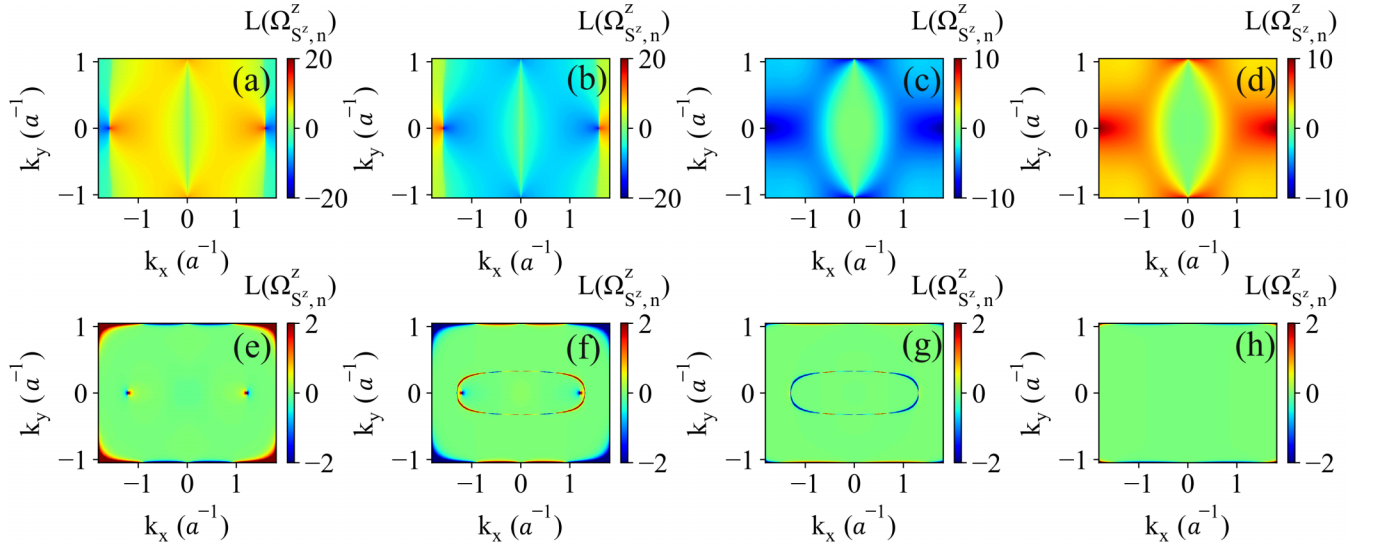


FIG. 5. The *spin* Berry curvature  $\Omega_{S_z, n}^z$  [Eq. (14)] computed for magnon-phonon bands (Fig. 2) of FePS<sub>3</sub> as a function of the in-plane wave vector  $(k_x, k_y)$  within the first BZ and in the absence of applied magnetic field  $B_z = 0$ . (a)–(h) correspond to bands 1–8 denoted in Fig. 2. The color bar encodes the magnitude of the function  $L = \text{sgn}(\Omega_{S_z, n}^z) \ln(1 + |\Omega_{S_z, n}^z|)$ .

eighth bands in Fig. 2(a) generates a finite Berry curvature at  $k_y \approx \pm 1$  ( $a^{-1}$ ) for the eighth (phononlike) band, as confirmed by Fig. 4(h).

Another consequence of these phonon-mediated magnon-magnon and magnon-mediated phonon-phonon interband transitions is that they induce the topological transverse transport of spin angular momentum carried by magnons with substantial spin Nernst conductivity even at *zero* applied magnetic field. Figure 5 shows the computed spin (generalized) Berry curvature [Eq. (5)] for bands 1–8 (Fig. 2) calculated for  $B_z = 0$ . We note that in the absence of both applied magnetic field and magnon-phonon coupling, the magnon bands exhibit a double degeneracy, with one set of bands carrying spin up [such as the first band in Fig. 2(a)] and another set carrying spin down [such as the second band in Fig. 2(a)]. Consequently, the band structures of the magnon-phonon system in FePS<sub>3</sub> also exhibit a double degeneracy, as illustrated in Fig. 2(b). However, the magnetoelastic coupling between the magnetic and elastic degrees of freedom in FePS<sub>3</sub> lifts the degeneracy of these two magnon bands with opposite spin, therefore making possible interband transition between these two magnonlike bands of opposite spin, even in the absence of an applied magnetic field (see the SM [58] for Fig. S3 and details of the calculations). Such phonon-mediated interband transitions between magnonlike bands, which are energetically distant from the usually considered [27–30] anticrossing regions [Fig. 3(a)] of hybridized magnon-phonon bands, can result in the very large spin Berry curvature found in Figs. 5(a)–5(d) because of the smallness [31] [with respect to the gap in anticrossing regions in Fig. 3(a)] of the energy gap between the two magnonlike bands with opposite spin polarization (Fig. S3(b) in the SM [58]). The same effect can operate between phononlike bands. For example, the seventh and eighth (phononlike) bands in Fig. 2(a) will exhibit magnon-mediated interband transitions, thereby developing finite spin Berry curvature [Figs. 5(g) and 5(h)].

## B. Magnetic field dependence of the thermal Hall and spin Nernst effects on applied magnetic field

Using computed Berry (Fig. 4) and spin Berry (Fig. 5) curvatures, we can obtain directly the thermal Hall [via Eq. (9)] and spin Nernst [via Eq. (10)] conductivities shown in Figs. 6(a) and 6(b), respectively, as a function of applied

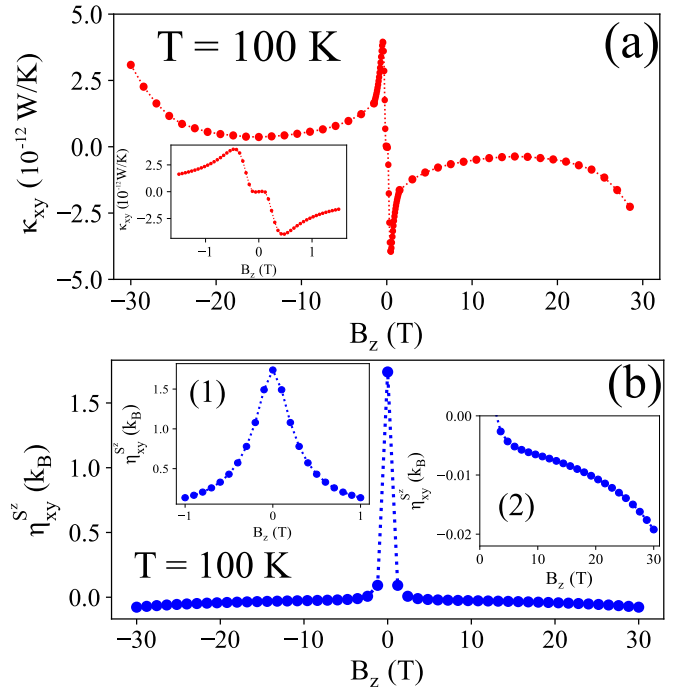


FIG. 6. (a) Thermal Hall and (b) spin Nernst conductivities as a function of applied magnetic field  $B_z$ . These conductivities are calculated at  $T = 100$  K using the FePS<sub>3</sub> magnon-phonon band structure (Fig. 2) and its Berry (Fig. 4) and spin Berry (Fig. 5) curvatures. The inset in (a) shows a zoom for  $B_z \in [-1.5 \text{ T}, 1.5 \text{ T}]$ . The two insets in (b) show zooms for (1)  $B_z \in [-1 \text{ T}, 1 \text{ T}]$  and (2)  $B_z \in [2 \text{ T}, 30 \text{ T}]$ .

magnetic field at a fixed temperature  $T = 100$  K that is below the Néel temperature of FePS<sub>3</sub>. We focus first on the behavior over a wide range of magnetic fields. As expected, the thermal Hall conductivity changes sign when we reverse the applied magnetic field, i.e.,  $\kappa_{xy}(B_z) = -\kappa_{xy}(-B_z)$ . In the absence of applied magnetic field [ $B_z = 0$  point in Fig. 6(a)], the thermal Hall conductivity vanishes. We can understand this feature by recognizing that when the applied magnetic field is absent, the system will be invariant under the time-reversal symmetry operation  $\mathcal{T}$  combined with the spin rotation symmetry operation  $\mathcal{C}$  that flips all spins in the system. The combination of these operations leads to an effective time-reversal symmetry (TRS) operation  $\mathcal{T}' = \mathcal{TC}$  under which  $\partial_x T$  is preserved while the thermal Hall current is transformed as  $j_y^Q \rightarrow -j_y^Q$ . Because this system preserves  $\mathcal{T}' = \mathcal{TC}$  symmetry,  $j_y^Q = -j_y^Q = 0$  and the thermal Hall conductivity  $\kappa_{xy}$  must be zero. We note that even though the thermal Hall conductivity  $\kappa_{xy}$  of the magnon-phonon hybridized system is zero at zero magnetic field, the Berry curvature  $\Omega_n^z(\mathbf{k})$  of individual bands may be finite at specific  $k$  points within the BZ, as long as the integral of the Berry curvature over the entire BZ vanishes (see the SM [58] for a detailed argument). This ensures that the THE induced by the magnon-phonon hybridization does not occur without breaking the effective TRS [29].

In the regime of small applied magnetic fields ( $B_z \in [-1.5 \text{ T}, 1.5 \text{ T}]$ ) the thermal Hall conductivity is primarily influenced by the phonon-mediated magnon-magnon interband transition. Here, the interplay between magnetoelastic coupling and the applied magnetic field results in intriguing nonlinear behaviors of the thermal Hall conductivity, as shown in the inset of Fig. 6(a). At very low applied magnetic fields ( $B_z \in [-0.1 \text{ T}, 0.1 \text{ T}]$ ), the thermal Hall conductivity exhibits a weak, but nonzero, dependence on the magnetic field  $B_z$ . For magnetic field magnitudes between  $|B_z| = 0.1 \text{ T}$  and  $|B_z| = 0.6 \text{ T}$  the thermal Hall conductivity exhibits a much stronger dependence on the magnitude of  $B_z$ , reaching a remarkably large value of approximately  $4 \times 10^{-12} \text{ W/K}$  at  $B_z \approx 0.6 \text{ T}$ . For magnetic field magnitudes larger than  $B_z \approx 0.6 \text{ T}$  the thermal Hall conductivity starts to decrease as a function of the magnitude of  $B_z$ . This nonlinear behavior can be attributed to the interplay of two distinct effects: (1) The first effect is the breaking of time-reversal symmetry. The breaking of time-reversal symmetry contributes to the increase in thermal Hall conductivity with respect to the external magnetic field. This effect dominates at small magnetic fields and leads to the initial rise in the thermal Hall conductivity as the magnitude of  $B_z$  increases from zero. (2) The second effect is the gap between opposite-spin magnonlike bands. The gap between the two magnonlike bands possessing opposite spin increases as the magnetic field strength increases. Consequently, the interband transition between magnonlike bands decreases, and this effect becomes more pronounced as the magnetic field magnitude increases. As a result of the decreasing interband transition, the thermal Hall conductivity starts to decline when the applied magnetic field exceeds 0.6 T. At even higher magnetic fields, typically above 5 T, the hybridization between the magnon and phonon modes comes into play. This hybridization effect significantly contributes to the thermal Hall conductivity and dominates the increase in thermal Hall

conductivity for magnetic field magnitudes larger than approximately 10 T.

In contrast to the thermal Hall conductivity, the spin Nernst conductivity shown in Fig. 6(b) is an even function of  $B_z$ , i.e.,  $\eta_{xy}^{S^z}(B_z) = \eta_{xy}^{S^z}(-B_z)$ . Moreover, the spin Nernst conductivity can be finite even in the absence of an applied magnetic field [31], i.e., under the effective time-reversal symmetry  $\mathcal{T}'$ . Indeed, if we rewrite the thermal spin current [Eq. (8)] as  $j_y^{S^z} = j_y^{S^z\uparrow} - j_y^{S^z\downarrow}$ , then under the  $\mathcal{T}'$  operation the spin-polarized currents on the right side change the sign and flip the spin, i.e.,  $\mathcal{T}' j_y^{S^z\uparrow} = -j_y^{S^z\downarrow}$  and  $\mathcal{T}' j_y^{S^z\downarrow} = -j_y^{S^z\uparrow}$ . This leads to  $\mathcal{T}' j_y^{S^z} = -j_y^{S^z\downarrow} + j_y^{S^z\uparrow} = j_y^{S^z}$ , which is always true because our system preserves the effective time-reversal symmetry in the absence of an applied magnetic field. It is therefore possible for the spin Nernst conductivity to be nonzero at zero applied magnetic field, as confirmed in Fig. 6(b). At zero or small applied magnetic field, the *giant* spin Nernst conductivity is mainly governed by phonon-mediated interband transitions between magnonlike bands. It then decays rapidly [inset (1) in Fig. 6] when the applied magnetic field is  $B_z \gtrsim 2 \text{ T}$ , dropping eventually by two orders of magnitude, because the energy spacing between the two magnonlike bands increases and thus interband transitions between the two are suppressed.

As the applied magnetic field magnitude increases from  $\approx 2$  to 30 T, the spin Nernst conductivity slightly changes while becoming negative,  $\eta_{xy}^{S^z} < 0$  [inset (2) in Fig. 6]. We find that from  $\approx 2$  to  $\approx 5 \text{ T}$ , the spin Nernst conductivity originates primarily from magnon-mediated interband transitions between phononlike bands. Once the phonon bands start hybridizing with magnon bands at  $B_z \approx 5 \text{ T}$ , the spin Berry curvature (Fig. 3) at anticrossing regions of magnon-phonon bands also contribute, as amply explored in prior literature [27–30]. To understand why the spin Nernst conductivity becomes more negative with increasing applied magnetic field, we consider that in the conserved spin approximation the spin Nernst conductivity derived from semiclassical theory is given by [28,55,75]

$$\eta_{xy}^{S^z} = -\frac{k_B}{\hbar V} \sum_k \sum_{n=1}^N \langle S^z \rangle_n \Omega_n^z F_1(E_n/k_B T), \quad (19)$$

where  $\langle S^z \rangle_n$  is the expectation value of the  $S^z$  operator in the  $n$ th magnon state,  $\Omega_n^z$  is the Berry curvature of the  $n$ th band, and the  $F_1$  function was defined in Eq. (11). From Eq. (19), we see that increasing the applied magnetic field leads to both larger spin polarization and stronger hybridizations between magnon and phonon states due to the shift toward energy degeneracy of the magnon and phonon states. Consequently, the amplitude of the spin Nernst conductivity  $\eta_{xy}^{S^z}$  is augmented within this regime.

Because the computed spin Nernst conductivity of FePS<sub>3</sub> around zero applied magnetic field is two orders of magnitude (Fig. 6) larger than at  $B_z \approx 10 \text{ T}$ , it should be possible to experimentally probe this effect by sweeping the magnetic field. Moreover, the spin Nernst conductivity (SNC) of FePS<sub>3</sub> predicted in this paper is approximately *four orders of magnitude* larger than the SNC recently reported for other

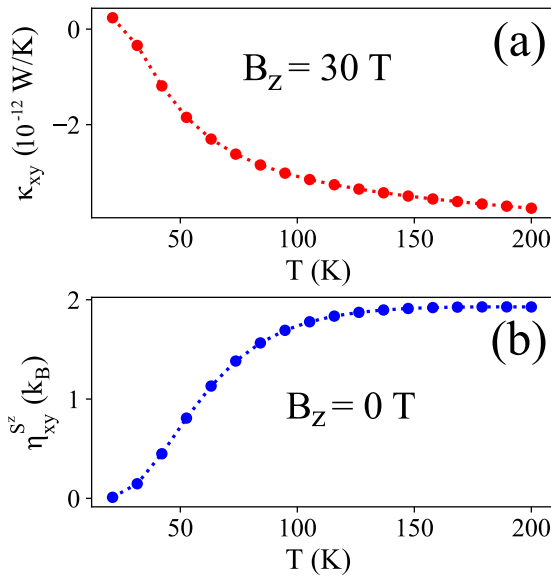


FIG. 7. (a) Thermal Hall and (b) spin Nernst conductivities of  $\text{FePS}_3$  as a function of temperature  $T$  calculated for applied magnetic field  $B_z = 30$  T in (a) or  $B_z = 0$  T in (b).

2D antiferromagnetic (AFM) materials such as the kagome antiferromagnet  $\text{KFe}_3(\text{OH})_6(\text{SO}_4)$  [47] and the collinear antiferromagnet  $\text{MnPS}_3$  in the Néel phase [30,55]. The SNC we compute for  $\text{FePS}_3$  is also *approximately five times larger* than the SNC reported recently for  $\text{CrSiTe}_3$ , which itself had the largest SNC among the other materials studied in Ref. [30]. From this comparison we see that  $\text{FePS}_3$  has a giant SNC in comparison to other 2D AFM materials, which could have significant implications for spintronics and related applications.

We also emphasize that in the absence of magnetoelastic coupling, both the thermal Hall and spin Nernst conductivities vanish, irrespective of the applied magnetic field. This is because the system without magnetoelastic coupling preserves  $\mathcal{T}_a\mathcal{M}_y$  symmetry, where  $\mathcal{M}_y$  is the mirror symmetry about the plane normal to the  $y$  axis and  $\mathcal{T}_a$  is a translation operator that moves the system by the vector  $\beta_2$  (Fig. 1). Unlike the effective time-reversal symmetry  $\mathcal{T}'$ ,  $\mathcal{T}_a\mathcal{M}_y$  does not change the spin direction but does change the sign of both the thermal Hall and thermal spin Nernst current. In other words, one must have  $j_y^Q = -j_y^Q = 0$  and  $j_y^{S^z} = -j_y^{S^z} = 0$ ; therefore both the thermal Hall and spin Nernst conductivity must be zero. It is only when the magnetoelastic interaction breaks  $\mathcal{T}_a\mathcal{M}_y$  symmetry that one obtains finite topological transverse transport of quasiparticles and their spin in a 2D AFM material.

Finally, Fig. 7 shows the thermal Hall and spin Nernst conductivities as a function of temperature using  $B_z = 30$  T or  $B_z = 0$  applied magnetic field, respectively. Both conductivities increase in magnitude with increasing temperature because there are increasing contributions to Berry and spin Berry curvature from phonon and magnon bands at higher energy. They start to saturate at  $T \simeq 100$  K when all magnon bands at higher energy have already been included. We note that when  $T \simeq 0$  K, the spin Nernst conductivity is almost zero, while the thermal Hall conductivity changes from positive to negative. This is because at very low temperature the main contributions to the THE come from the acoustic phonon band [the eighth band in Fig. 2(a)] with positive Chern number  $C_8 = 1$  [Fig. 4(h)]. As the temperature increases even slightly, the other bands with negative Chern number begin to contribute to topological transverse transport of quasiparticles, and thus the thermal Hall conductivity becomes negative. In contrast, even though the spin Berry curvature of the lowest phononlike band [the eighth band in Fig. 2(a)] is finite, the sum of the spin Berry curvature of the eighth band over the entire BZ vanishes to yield  $\eta_{xy}^{S^z} \rightarrow 0$  at zero temperature.

#### IV. CONCLUSIONS

In conclusion, we have investigated the transverse topological transport of magnon-polaron quasiparticles in the zigzag phase of the  $\text{FePS}_3$  2D AFM. While we reproduce previous findings [27–30], obtained for different realizations of 2D AFMs, on the magnetoelastic coupling mechanism where anticrossing regions of hybridized magnon-phonon bands provide key contributions [28] to the THE and SNE, we also predict a giant spin Nernst current carried by magnons even in zero applied magnetic field. This surprising finding was noticed before [31], but here we explain it thoroughly by using perturbative equation (18), which reveals that the principal contribution to the spin Berry curvature behind the SNE comes from the interband transition between slightly gapped magnonlike bands that are far away in energy from the usually considered anticrossing regions [27–30]. Of relevance to experimental probing of the THE and SNE, which is currently lacking [27], our analysis indicates that  $\text{FePS}_3$  will exhibit sizable thermal Hall conductivity and giant spin Nernst conductivities at temperatures  $T \simeq 100$  K, which is still below its Néel temperature  $T_N \approx 118$  K [49,84].

#### ACKNOWLEDGMENT

This research was primarily supported by NSF through the University of Delaware Materials Research Science and Engineering Center, Grant No. DMR-2011824.

- [1] M. Gibertini, M. Koperski, A. F. Morpurgo, and K. S. Novoselov, Magnetic 2D materials and heterostructures, *Nat. Nanotechnol.* **14**, 408 (2019).  
 [2] M. B. Jungfleisch, W. Zhang, and A. Hoffmann, Perspectives of antiferromagnetic spintronics, *Phys. Lett. A* **382**, 865 (2018).

- [3] L. Hao, D. Meyers, H. Suwa, J. Yang, C. Frederick, T. R. Dasa, G. Fabbris, L. Horak, D. Kriegner, Y. Choi, J.-W. Kim, D. Haskel, P. J. Ryan, H. Xu, C. D. Batista, M. P. M. Dean, and J. Liu, Giant magnetic response of a two-dimensional antiferromagnet, *Nat. Phys.* **14**, 806 (2018).



- [4] B. Huang, M. A. McGuire, A. F. May, D. Xiao, P. Jarillo-Herrero, and X. Xu, Emergent phenomena and proximity effects in two-dimensional magnets and heterostructures, *Nat. Mater.* **19**, 1276 (2020).
- [5] K. Dolui, M. D. Petrovic, K. Zollner, P. Plechac, J. Fabian, and B. K. Nikolić, Proximity spin-orbit torque on a two-dimensional magnet within van der Waals heterostructure: Current-driven antiferromagnet-to-ferromagnet reversible nonequilibrium phase transition in bilayer CrI<sub>3</sub>, *Nano Lett.* **20**, 2288 (2020).
- [6] S. Yang, T. Zhang, and C. Jiang, van der Waals magnets: Material family, detection and modulation of magnetism, and perspective in spintronics, *Adv. Sci.* **8**, 2002488 (2021).
- [7] X. Jiang, Q. Liu, J. Xing, N. Liu, Y. Guo, Z. Liu, and J. Zhao, Recent progress on 2D magnets: Fundamental mechanism, structural design and modification, *Appl. Phys. Rev.* **8**, 031305 (2021).
- [8] X. Tan, L. Ding, G.-F. Du, and H.-H. Fu, Spin caloritronics in two-dimensional CrI<sub>3</sub>/NiCl<sub>2</sub> van der Waals heterostructures, *Phys. Rev. B* **103**, 115415 (2021).
- [9] M.-H. Phan, M. T. Trinh, T. Eggers, V. Kalappattil, K.-i. Uchida, L. M. Woods, and M. Terrones, A perspective on two-dimensional van der Waals opto-spin-caloritronics, *Appl. Phys. Lett.* **119**, 250501 (2021).
- [10] D. Xiong, Y. Jiang, K. Shi, A. Du, Y. Yao, Z. Guo, D. Zhu, K. Cao, S. Peng, W. Cai, D. Zhu, and W. Zhao, Antiferromagnetic spintronics: An overview and outlook, *Fundam. Res.* **2**, 522 (2022).
- [11] A. Suresh, U. Bajpai, and B. K. Nikolić, Magnon-driven chiral charge and spin pumping and electron-magnon scattering from time-dependent quantum transport combined with classical atomistic spin dynamics, *Phys. Rev. B* **101**, 214412 (2020).
- [12] X.-X. Zhang, L. Li, D. Weber, J. Goldberger, K. F. Mak, and J. Shan, Gate-tunable spin waves in antiferromagnetic atomic bilayers, *Nat. Mater.* **19**, 838 (2020).
- [13] A. Suresh, U. Bajpai, M. D. Petrović, H. Yang, and B. K. Nikolić, Magnon- versus Electron-Mediated Spin-Transfer Torque Exerted by Spin Current across an Antiferromagnetic Insulator to Switch the Magnetization of an Adjacent Ferromagnetic Metal, *Phys. Rev. Appl.* **15**, 034089 (2021).
- [14] U. Bajpai, A. Suresh, and B. K. Nikolić, Quantum many-body states and Green's functions of nonequilibrium electron-magnon systems: Localized spin operators versus their mapping to Holstein-Primakoff bosons, *Phys. Rev. B* **104**, 184425 (2021).
- [15] C. A. Belvin, E. Baldini, I. O. Ozel, D. Mao, H. C. Po, C. J. Allington, S. Son, B. H. Kim, J. Kim, I. Hwang, J. H. Kim, J.-G. Park, T. Senthil, and N. Gedik, Exciton-driven antiferromagnetic metal in a correlated van der Waals insulator, *Nat. Commun.* **12**, 4837 (2021).
- [16] A. V. Chumak, P. Kabos, M. Wu, C. Abert, C. Adelman, A. Adeyeye, J. Åkerman, F. G. Aliev, A. Anane, A. Awad, C. H. Back, A. Barman, G. E. W. Bauer, M. Becherer, E. N. Beginin, V. A. S. V. Bittencourt, Y. M. Blanter, P. Bortolotti, I. Boventer, D. A. Bozhko *et al.*, Advances in magnetics roadmap on spin-wave computing, *IEEE Trans. Magn.* **58**, 1 (2022).
- [17] J. Li, H. T. Simensen, D. Reitz, Q. Sun, W. Yuan, C. Li, Y. Tserkovnyak, A. Brataas, and J. Shi, Observation of Magnon Polarons in a Uniaxial Antiferromagnetic Insulator, *Phys. Rev. Lett.* **125**, 217201 (2020).
- [18] R. Yahiro, T. Kikkawa, R. Ramos, K. Oyanagi, T. Hioki, S. Daimon, and E. Saitoh, Magnon polarons in the spin Peltier effect, *Phys. Rev. B* **101**, 024407 (2020).
- [19] N. Vidal-Silva, E. Aguilera, A. Roldán-Molina, R. A. Duine, and A. S. Nunez, Magnon polarons induced by a magnetic field gradient, *Phys. Rev. B* **102**, 104411 (2020).
- [20] S. M. Tabatabaei, R. A. Duine, and B. Zare Rameshti, Magnon-polaron anomaly in nonlocal spin transport through antiferromagnetic insulators, *Phys. Rev. B* **104**, 014432 (2021).
- [21] T. Kikkawa, K. Oyanagi, T. Hioki, M. Ishida, Z. Qiu, R. Ramos, Y. Hashimoto, and E. Saitoh, Composition-tunable magnon-polaron anomalies in spin Seebeck effects in epitaxial Bi<sub>x</sub>Y<sub>3-x</sub>Fe<sub>5</sub>O<sub>12</sub> films, *Phys. Rev. Mater.* **6**, 104402 (2022).
- [22] W. Chen and M. Sigrist, Dissipationless Multiferroic Magnonics, *Phys. Rev. Lett.* **114**, 157203 (2015).
- [23] T. Nomura, X.-X. Zhang, S. Zherlitsyn, J. Wosnitza, Y. Tokura, N. Nagaosa, and S. Seki, Phonon Magnetochiral Effect, *Phys. Rev. Lett.* **122**, 145901 (2019).
- [24] C. Zhao, Y. Li, Z. Zhang, M. Vogel, J. E. Pearson, J. Wang, W. Zhang, V. Novosad, Q. Liu, and A. Hoffmann, Phonon Transport Controlled by Ferromagnetic Resonance, *Phys. Rev. Appl.* **13**, 054032 (2020).
- [25] J. Holanda, D. S. Maior, O. A. Santos, A. Azevedo, and S. M. Rezende, Evidence of phonon pumping by magnonic spin currents, *Appl. Phys. Lett.* **118**, 022409 (2021).
- [26] S. M. Rezende, D. S. Maior, O. Alves Santos, and J. Holanda, Theory for phonon pumping by magnonic spin currents, *Phys. Rev. B* **103**, 144430 (2021).
- [27] H. Zhang and R. Cheng, A perspective on magnon spin Nernst effect in antiferromagnets, *Appl. Phys. Lett.* **120**, 090502 (2022).
- [28] S. Park, N. Nagaosa, and B.-J. Yang, Thermal Hall effect, spin Nernst effect, and spin density induced by a thermal gradient in collinear ferrimagnets from magnon-phonon interaction, *Nano Lett.* **20**, 2741 (2020).
- [29] S. Zhang, G. Go, K.-J. Lee, and S. K. Kim, SU(3) Topology of Magnon-Phonon Hybridization in 2D Antiferromagnets, *Phys. Rev. Lett.* **124**, 147204 (2020).
- [30] N. Bazazzadeh, M. Hamdi, S. Park, A. Khavasi, S. M. Mohseni, and A. Sadeghi, Magnetoelastic coupling enabled tunability of magnon spin current generation in two-dimensional antiferromagnets, *Phys. Rev. B* **104**, L180402 (2021).
- [31] G. Go and S. K. Kim, Tunable large spin Nernst effect in a two-dimensional magnetic bilayer, *Phys. Rev. B* **106**, 125103 (2022).
- [32] Q. Zhang, M. Ozerov, E. V. Boström, J. Cui, N. Suri, Q. Jiang, C. Wang, F. Wu, K. Hwangbo, J.-H. Chu, D. Xiao, A. Rubio, and X. Xu, Coherent strong-coupling of terahertz magnons and phonons in a van der Waals antiferromagnetic insulator, *arXiv:2108.11619v1*.
- [33] J. Luo, S. Li, Z. Ye, R. Xu, H. Yan, J. Zhang, G. Ye, L. Chen, D. Hu, X. Teng, W. A. Smith, B. I. Yakobson, P. Dai, A. H. Nevidomskyy, R. He, and H. Zhu, Evidence for topological magnon-phonon hybridization in a 2D antiferromagnet down to the monolayer limit, *Nano Lett.* **23**, 2023 (2023).
- [34] M. Xu, J. Puebla, F. Auvray, B. Rana, K. Kondou, and Y. Otani, Inverse Edelstein effect induced by magnon-phonon coupling, *Phys. Rev. B* **97**, 180301(R) (2018).
- [35] F. Godejohann, A. V. Scherbakov, S. M. Kukhtaruk, A. N. Poddubny, D. D. Yaremkevich, M. Wang, A. Nadzeyka,

- D. R. Yakovlev, A. W. Rushforth, A. V. Akimov, and M. Bayer, Magnon polaron formed by selectively coupled coherent magnon and phonon modes of a surface patterned ferromagnet, *Phys. Rev. B* **102**, 144438 (2020).
- [36] C. R. Berk and H. Schmidt, A quantum tango between magnons and phonons, *Physics* **13**, 167 (2020).
- [37] D. Bozhko, V. Vasyuchka, A. Chumak, and A. Serga, Magnon-phonon interactions in magnon spintronics, *Low Temp. Phys.* **46**, 383 (2020).
- [38] D. D. Awschalom, C. R. Du, R. He, F. J. Heremans, A. Hoffmann, J. Hou, H. Kurebayashi, Y. Li, L. Liu, V. Novosad, J. Sklenar, S. E. Sullivan, D. Sun, H. Tang, V. Tyberkevych, C. Trevillian, A. W. Tsen, L. R. Weiss, W. Zhang, X. Zhang *et al.*, Quantum engineering with hybrid magnonic systems and materials, *IEEE Trans. Quantum Eng.* **2**, 1 (2021).
- [39] Y. Li, C. Zhao, W. Zhang, A. Hoffmann, and V. Novosad, Advances in coherent coupling between magnons and acoustic phonons, *APL Mater.* **9**, 060902 (2021).
- [40] F. Mertens, D. Mönkebücher, U. Parlak, C. Boix-Constant, S. Mañas-Valero, M. Matzer, R. Adhikari, A. Bonanni, E. Coronado, A. M. Kalashnikova, D. Bossini, and M. Cinchetti, Ultrafast coherent THz lattice dynamics coupled to spins in the van der Waals antiferromagnet FePS<sub>3</sub>, *Adv. Mater.* **35**, 2208355 (2023).
- [41] V. A. Zyuzin and A. A. Kovalev, Magnon Spin Nernst Effect in Antiferromagnets, *Phys. Rev. Lett.* **117**, 217203 (2016).
- [42] R. Takahashi and N. Nagaosa, Berry Curvature in Magnon-Phonon Hybrid Systems, *Phys. Rev. Lett.* **117**, 217205 (2016).
- [43] S. Murakami and A. Okamoto, Thermal Hall effect of magnons, *J. Phys. Soc. Jpn.* **86**, 011010 (2017).
- [44] G. Go, S. K. Kim, and K.-J. Lee, Topological Magnon-Phonon Hybrid Excitations in Two-Dimensional Ferromagnets with Tunable Chern Numbers, *Phys. Rev. Lett.* **123**, 237207 (2019).
- [45] X. Zhang, Y. Zhang, S. Okamoto, and D. Xiao, Thermal Hall Effect Induced by Magnon-Phonon Interactions, *Phys. Rev. Lett.* **123**, 167202 (2019).
- [46] A. Okamoto, S. Murakami, and K. Everschor-Sitte, Berry curvature for magnetoelastic waves, *Phys. Rev. B* **101**, 064424 (2020).
- [47] B. Li, S. Sandhoefner, and A. A. Kovalev, Intrinsic spin Nernst effect of magnons in a noncollinear antiferromagnet, *Phys. Rev. Res.* **2**, 013079 (2020).
- [48] B. Ma and G. A. Fiete, Antiferromagnetic insulators with tunable magnon-polaron Chern numbers induced by in-plane optical phonons, *Phys. Rev. B* **105**, L100402 (2022).
- [49] S. Liu, A. Granados del Águila, D. Bhowmick, C. K. Gan, T. Thu Ha Do, M. A. Prosnikov, D. Sedmidubský, Z. Sofer, P. C. M. Christianen, P. Sengupta, and Q. Xiong, Direct Observation of Magnon-Phonon Strong Coupling in Two-Dimensional Antiferromagnet at High Magnetic Fields, *Phys. Rev. Lett.* **127**, 097401 (2021).
- [50] D. Vaclavkova, M. Palit, J. Wyzula, S. Ghosh, A. Delhomme, S. Maity, P. Kapuscinski, A. Ghosh, M. Veis, M. Grzeszczyk, C. Faugeras, M. Orlita, S. Datta, and M. Potemski, Magnon polarons in the van der Waals antiferromagnet FePS<sub>3</sub>, *Phys. Rev. B* **104**, 134437 (2021).
- [51] A. Pawbake, T. Pelini, A. Delhomme, D. Romanin, D. Vaclavkova, G. Martinez, M. Calandra, M.-A. Measson, M. Veis, M. Potemski, M. Orlita, and C. Faugeras, High-pressure tuning of magnon-polarons in the layered antiferromagnet FePS<sub>3</sub>, *ACS Nano* **16**, 12656 (2022).
- [52] Y.-J. Sun, J.-M. Lai, S.-M. Pang, X.-L. Liu, P.-H. Tan, and J. Zhang, Magneto-Raman study of magnon-phonon coupling in two-dimensional Ising antiferromagnetic FePS<sub>3</sub>, *J. Phys. Chem. Lett.* **13**, 1533 (2022).
- [53] J. Sinova, S. O. Valenzuela, J. Wunderlich, C. H. Back, and T. Jungwirth, Spin Hall effects, *Rev. Mod. Phys.* **87**, 1213 (2015).
- [54] B. K. Nikolić, L. P. Zárbo, and S. Souma, Imaging mesoscopic spin Hall flow: Spatial distribution of local spin currents and spin densities in and out of multiterminal spin-orbit coupled semiconductor nanostructures, *Phys. Rev. B* **73**, 075303 (2006).
- [55] R. Cheng, S. Okamoto, and D. Xiao, Spin Nernst Effect of Magnons in Collinear Antiferromagnets, *Phys. Rev. Lett.* **117**, 217202 (2016).
- [56] S. E. Hog, H. T. Diep, and H. Puzkarski, Theory of magnons in spin systems with Dzyaloshinskii-Moriya interaction, *J. Phys.: Condens. Matter* **29**, 305001 (2017).
- [57] A. Mook, R. R. Neumann, J. Henk, and I. Mertig, Spin Seebeck and spin Nernst effects of magnons in noncollinear antiferromagnetic insulators, *Phys. Rev. B* **100**, 100401(R) (2019).
- [58] See Supplemental Material at <http://link.aps.org/supplemental/10.1103/PhysRevB.108.085435> for (i) the magnon-phonon Hamiltonian in the second-quantization formalism and details of its exact diagonalization; (ii) the physical interpretation of the gap opening [Eq. (18)] between two magnonlike bands energetically distant from anticrossing regions, as found in exact diagonalization, by using perturbation from phonons onto magnons examined via the Löwdin partitioning; and (iii) additional details of Berry and spin Berry curvature calculations and related symmetry arguments. It also contain Refs. [85–96].
- [59] T. Olsen, Theory and simulations of critical temperatures in CrI<sub>3</sub> and other 2D materials: easy-axis magnetic order and easy-plane Kosterlitz-Thouless transitions, *MRS Commun.* **9**, 1142 (2019).
- [60] J. Vanherck, C. Bacaksiz, B. Sorée, M. V. Milošević, and W. Magnus, 2D ferromagnetism at finite temperatures under quantum scrutiny, *Appl. Phys. Lett.* **117**, 052401 (2020).
- [61] T. Olsen, Magnetic anisotropy and exchange interactions of two-dimensional FePS<sub>3</sub>, NiPS<sub>3</sub> and MnPS<sub>3</sub> from first principles calculations, *J. Phys. D: Appl. Phys.* **54**, 314001 (2021).
- [62] K.-Z. Du, X.-Z. Wang, Y. Liu, P. Hu, M. I. B. Utama, C. K. Gan, Q. Xiong, and C. Kloc, Weak van der Waals stacking, wide-range band gap, and raman study on ultrathin layers of metal phosphorus trichalcogenides, *ACS Nano* **10**, 1738 (2016).
- [63] J.-U. Lee, S. Lee, J. H. Ryoo, S. Kang, T. Y. Kim, P. Kim, C.-H. Park, J.-G. Park, and H. Cheong, Ising-type magnetic ordering in atomically thin FePS<sub>3</sub>, *Nano Lett.* **16**, 7433 (2016).
- [64] J. Cui, E. V. Bostrom, M. Ozerov, F. Wu, Q. Jiang, J.-H. Chu, C. Li, F. Liu, X. Xu, A. Rubio, and Q. Zhang, Chirality selective magnon-phonon hybridization and magnon-induced chiral phonons in an atomically thin antiferromagnet, *Nat. Commun.* **14**, 3396 (2023).
- [65] A. Wildes, K. C. Rule, R. Bewley, M. Enderle, and T. J. Hicks, The magnon dynamics and spin exchange parameters of FePS<sub>3</sub>, *J. Phys.: Condens. Matter* **24**, 416004 (2012).
- [66] D. Laçon, H. C. Walker, E. Ressouche, B. Ouladidaf, K. C. Rule, G. J. McIntyre, T. J. Hicks, H. M. Rønnow, and A. R. Wildes, Magnetic structure and magnon dynamics of the

- quasi-two-dimensional antiferromagnet FePS<sub>3</sub>, *Phys. Rev. B* **94**, 214407 (2016).
- [67] D. Q. To, W. Wu, S. Bhatt, Y. Liu, A. Janotti, J. M. O. Zide, M. J. H. Ku, J. Q. Xiao, M. B. Jungfleisch, S. Law, and M. F. Doty, Phonon-mediated strong coupling between a three-dimensional topological insulator and a two-dimensional antiferromagnetic material, *Phys. Rev. Mater.* **7**, 045201 (2023).
- [68] R. Basnet, K. M. Kotur, M. Rybak, C. Stephenson, S. Bishop, C. Autieri, M. Birowska, and J. Hu, Controlling magnetic exchange and anisotropy by nonmagnetic ligand substitution in layered MPX<sub>3</sub> ( $M = \text{Ni, Mn}$ ;  $X = \text{S, Se}$ ), *Phys. Rev. Res.* **4**, 023256 (2022).
- [69] K. Zollner and J. Fabian, Proximity effects in graphene on monolayers of transition-metal phosphorus trichalcogenides MPX<sub>3</sub> ( $M : \text{Mn, Fe, Ni, Co}$ , and  $X : \text{S, Se}$ ), *Phys. Rev. B* **106**, 035137 (2022).
- [70] Y. Lee, S. Son, C. Kim, S. Kang, J. Shen, M. Kenzelmann, B. Delley, T. Savchenko, S. Parchenko, W. Na, K.-Y. Choi, W. Kim, H. Cheong, P. M. Derlet, A. Kleibert, and J.-G. Park, Giant magnetic anisotropy in the atomically thin van der Waals antiferromagnet FePS<sub>3</sub>, *Adv. Electron. Mater.* **9**, 2200650 (2023).
- [71] P. Shen and S. K. Kim, Magnetic field control of topological magnon-polaron bands in two-dimensional ferromagnets, *Phys. Rev. B* **101**, 125111 (2020).
- [72] C. Kittel, Interaction of spin waves and ultrasonic waves in ferromagnetic crystals, *Phys. Rev.* **110**, 836 (1958).
- [73] H. T. Simensen, R. E. Troncoso, A. Kamra, and A. Brataas, Magnon-polarons in cubic collinear antiferromagnets, *Phys. Rev. B* **99**, 064421 (2019).
- [74] T. Sato, W. Yu, S. Streib, and G. E. W. Bauer, Dynamic magnetoelastic boundary conditions and the pumping of phonons, *Phys. Rev. B* **104**, 014403 (2021).
- [75] R. Matsumoto and S. Murakami, Theoretical Prediction of a Rotating Magnon Wave Packet in Ferromagnets, *Phys. Rev. Lett.* **106**, 197202 (2011).
- [76] R. Shindou, J.-i. Ohe, R. Matsumoto, S. Murakami, and E. Saitoh, Chiral spin-wave edge modes in dipolar magnetic thin films, *Phys. Rev. B* **87**, 174402 (2013).
- [77] R. Shindou, R. Matsumoto, S. Murakami, and J.-i. Ohe, Topological chiral magnonic edge mode in a magnonic crystal, *Phys. Rev. B* **87**, 174427 (2013).
- [78] R. Matsumoto, R. Shindou, and S. Murakami, Thermal Hall effect of magnons in magnets with dipolar interaction, *Phys. Rev. B* **89**, 054420 (2014).
- [79] J. H. P. Colpa, Diagonalization of the quadratic boson Hamiltonian, *Phys. A (Amsterdam)* **93**, 327 (1978).
- [80] J. H. P. Colpa, Diagonalisation of the quadratic fermion Hamiltonian with a linear part, *J. Phys. A: Math. Gen.* **12**, 469 (1979).
- [81] J. H. P. Colpa, Diagonalization of the quadratic boson Hamiltonian with zero modes: I. Mathematical, *Phys. A (Amsterdam)* **134**, 377 (1986).
- [82] J. H. P. Colpa, Diagonalization of the quadratic boson Hamiltonian with zero modes: II. Physical, *Phys. A (Amsterdam)* **134**, 417 (1986).
- [83] B. A. Bernevig, T. L. Hughes, and S.-C. Zhang, Quantum spin Hall effect and topological phase transition in HgTe quantum wells, *Science* **314**, 1757 (2006).
- [84] R. Basnet, A. Wegner, K. Pandey, S. Storment, and J. Hu, Highly sensitive spin-flop transition in antiferromagnetic van der Waals material MPS<sub>3</sub> ( $M = \text{Ni}$  and  $\text{Mn}$ ), *Phys. Rev. Mater.* **5**, 064413 (2021).
- [85] T. Holstein and H. Primakoff, Field dependence of the intrinsic domain magnetization of a ferromagnet, *Phys. Rev.* **58**, 1098 (1940).
- [86] P.-O. Löwdin, A note on the quantum-mechanical perturbation theory, *J. Chem. Phys.* **19**, 1396 (1951).
- [87] P.-O. Löwdin, Partitioning technique, perturbation theory, and rational approximations, *Int. J. Quantum Chem.* **21**, 69 (1982).
- [88] L. Jin and Z. Song, Partitioning technique for discrete quantum systems, *Phys. Rev. A* **83**, 062118 (2011).
- [89] J. R. Schrieffer and P. A. Wolff, Relation between the Anderson and Kondo Hamiltonians, *Phys. Rev.* **149**, 491 (1966).
- [90] S. Bravyi, D. P. DiVincenzo, and D. Loss, Schrieffer-Wolff transformation for quantum many-body systems, *Ann. Phys. (Amsterdam)* **326**, 2793 (2011).
- [91] Z. Zhou, L.-L. Wan, and Z.-F. Xu, Topological classification of excitations in quadratic bosonic systems, *J. Phys. A: Math. Theor.* **53**, 425203 (2020).
- [92] L.-L. Wan, Z. Zhou, and Z.-F. Xu, Squeezing-induced topological gap opening on bosonic Bogoliubov excitations, *Phys. Rev. A* **103**, 013308 (2021).
- [93] G. Massarelli, I. Khait, and A. Paramekanti, Krein-unitary Schrieffer-Wolff transformation and band touchings in bosonic Bogoliubov–de Gennes and other Krein-Hermitian Hamiltonians, *Phys. Rev. B* **106**, 144434 (2022).
- [94] T. Ohashi, S. Kobayashi, and Y. Kawaguchi, Generalized Berry phase for a bosonic Bogoliubov system with exceptional points, *Phys. Rev. A* **101**, 013625 (2020).
- [95] M. Amirabbasi and P. Kratzer, Orbital and magnetic ordering in single-layer FePS<sub>3</sub>: A DFT + $U$  study, *Phys. Rev. B* **107**, 024401 (2023).
- [96] R. M. White, M. Sparks, and I. Ortenburger, Diagonalization of the antiferromagnetic magnon-phonon interaction, *Phys. Rev.* **139**, A450 (1965).